

MIT Open Access Articles

*Cascade Defluorination of Perfluoroalkylated Catholytes
Unlocks High Lithium Primary Battery Capacities*

The MIT Faculty has made this article openly available. **Please share** how this access benefits you. Your story matters.

Citation: Gao, Haining, Yoshinaga, Kosuke, Steinberg, Katherine, Swager, Timothy M and Gallant, Betar M. 2023. "Cascade Defluorination of Perfluoroalkylated Catholytes Unlocks High Lithium Primary Battery Capacities." *Advanced Energy Materials*, 13 (32).

As Published: 10.1002/aenm.202301751

Publisher: Wiley

Persistent URL: <https://hdl.handle.net/1721.1/152314>

Version: Final published version: final published article, as it appeared in a journal, conference proceedings, or other formally published context

Terms of use: Creative Commons Attribution-Noncommercial-NoDerivatives



Cascade Defluorination of Perfluoroalkylated Catholytes Unlocks High Lithium Primary Battery Capacities

Haining Gao, Kosuke Yoshinaga, Katherine Steinberg, Timothy M. Swager, and Betar M. Gallant*

Exceeding the energy density of lithium–carbon monofluoride (Li–CF_x), today's leading Li primary battery, requires an increase in fluorine content (x) that determines the theoretical capacity available from C–F bond reduction. However, high F-content carbon materials face challenges such as poor electronic conductivity, low reduction potentials (<1.3 V versus Li/Li⁺), and/or low C–F bond utilization. This study investigates molecular structural design principles for a new class of high F-content fluoroalkyl-aromatic catholytes that address these challenges. A polarizable conjugated system—an aromatic ring with an alkene linker—functions as electron acceptor and redox initiator, enabling a cascade defluorination of an adjacent perfluoroalkyl chain ($R_F = -C_nF_{2n+1}$). The synthesized molecules successfully overcome premature deactivation observed in previously studied catholytes and achieve close-to-full defluorination (up to 15/17 available F), yielding high gravimetric capacities of 748 mAh g⁻¹ fluoroalkyl-aromatic and energies of 1785 Wh kg⁻¹ fluoroalkyl-aromatic. The voltage compatibility between fluoroalkyl-aromatics and CF_x enables design of hybrid cells containing C–F redox activity in both solid and liquid phases, with a projected enhancement of Li–CF_x gravimetric energy by 35% based on weight of electrodes+electrolyte. With further improvement of cathode architecture, these “liquid CF_x” analogues are strong candidates for exceeding the energy limitations of today's primary chemistries.

1. Introduction

Lithium (Li) primary (non-rechargeable) batteries are critical for long-duration powered applications where recharging is impractical or inessential, such as medical implants, unmanned vehicles, tracking devices, and sensors for the Internet of Things.^[1] Unlike rechargeable batteries that use transition metals (e.g., cobalt, nickel, manganese) and accommodate only 1–2 electrons transferred per redox center,^[2] primary battery cathodes employ light, non-transition metal redox centers such as carbon (C) or sulfur (S) as in Li–carbon monofluoride (Li–CF_x)^[3] or Li–thionyl chloride (Li–SOCl₂) batteries.^[4] The significantly lessened weight per charge transferred enables high cell-level energy density of up to 800 Wh kg⁻¹ packaged cell for Li–CF_x and 590 Wh kg⁻¹ packaged cell for Li–SOCl₂,^[5] which is two to three times higher than rechargeable Li-ion batteries (≈260 Wh kg⁻¹ packaged).^[6] At the active materials level, Li–CF_x ($0 < x \leq 1.3$) can reach up to 2180 Wh kg⁻¹ Li+CF_x (assuming $x = 1$).^[5] The solid nature


of CF_x particles also contributes to both good safety and long-term storage characteristics. However, to meet the ever-increasing energy and power requirements of electronic devices, further advancements in both intrinsic energy density and discharge rate capability of CF_x are needed. Research efforts have largely focused on improving CF_x performance at high discharge rates, which is limited by the poor electronic conductivity of CF_x.^[7] To address this challenge, researchers have pursued several strategies: 1) Optimizing the cathode architecture (e.g., adding carbon nanotubes) for improved electronic conductivity, which enabled CF_x discharge at >1 C rates^[8]; 2) Interrogating the CF_x reduction mechanism at atomic length scales to understand the origin of overpotentials, and to inform further material optimization;^[9] and 3) Decreasing fluorine (F) content, x , to 0.33–0.66 for improved electronic conductivity of CF_x particles,^[10] although this approach lowers the energy density.

In contrast, increasing the fluorine stoichiometry x has long been of interest as it also allows the theoretical energy of Li–CF_x (proportional to the degree of fluorination) to be increased by expanding the valence state change accessible on C. However,

H. Gao, B. M. Gallant
Department of Mechanical Engineering
Massachusetts Institute of Technology
77 Massachusetts Avenue, Cambridge, MA 02139, USA
E-mail: bgallant@mit.edu

K. Yoshinaga, T. M. Swager
Department of Chemistry
Massachusetts Institute of Technology
77 Massachusetts Avenue, Cambridge, MA 02139, USA

K. Steinberg
Department of Chemical Engineering
Massachusetts Institute of Technology
77 Massachusetts Avenue, Cambridge, MA 02139, USA

 The ORCID identification number(s) for the author(s) of this article can be found under <https://doi.org/10.1002/aenm.202301751>

© 2023 The Authors. Advanced Energy Materials published by Wiley-VCH GmbH. This is an open access article under the terms of the Creative Commons Attribution-NonCommercial-NoDerivs License, which permits use and distribution in any medium, provided the original work is properly cited, the use is non-commercial and no modifications or adaptations are made.

DOI: 10.1002/aenm.202301751

such superstoichiometric fluorination has been deemed unfavorable in practice because of the highly insulating nature of carbon when x exceeds 1.^[11] As a result, although it is possible for CF_x to maintain the desired layered lattice structure (similar to CF_1) at $x = 1.3$,^[12] the maximum F content in commercial Li– CF_x cells is still typically around 1 (theoretical capacity = 865 mAh $\text{g}^{-1}_{\text{CF}_x}$) or below,^[13] leaving the super-stoichiometric CF_x ($x > 1$) largely underutilized in practice. For solid fluorocarbon materials with an even higher F content ($x \geq 2$) such as polytetrafluoroethylene (PTFE, $(\text{C}_2\text{F}_4)_n$), the high covalent C–F bond energy ($\approx 485 \text{ kJ mol}^{-1}$)^[14] impedes electrochemical defluorination with reduction occurring only at low potentials ($< 1.3 \text{ V vs Li/Li}^+$).^[15]

Recently, we investigated the electrochemical performance of perfluoroalkylated liquid reactants that contain multiple C–F bond cleavage sites per C, with high F content (F/C mole ratio $x \geq 2$).^[16] Liquid perfluoroalkyl iodides ($\text{C}_n\text{F}_{2n+1}\text{I}$, termed “CFI”) were studied as exemplars of this class. Reactants were blended with 0.1 M lithium perchlorate (LiClO_4)/dimethyl sulfoxide (DMSO) electrolyte to yield a catholyte and were discharged in Li–carbon cells. Discharge voltages of up to 2.8 V versus Li/Li⁺ were observed alongside a high degree of electrochemical defluorination (8/13 total F reacted, or $\approx 8 \text{ e}^-$ transfer per CFI) at low reactant concentrations (0.1 M) and rates (0.02 mA cm^{-2}). The surprising degree of electrochemical activity of CFI, which is atypical for perfluoroalkyl reactants, was attributed to the inclusion of the large, polarizable iodine that weakens nearby C–F bonds and facilitates the initial electron transfer. Following this initiation, a sequential reduction and defluorination propagates along the R_F tail. C–F bond activity in those reactants was further observed to be governed by multiple factors, including supporting solvent properties, perfluoroalkyl group ($\text{R}_F = -\text{C}_n\text{F}_{2n+1}$) chain length, CFI reactant concentration (0.1–3 M), discharge rate, and temperature (room temperature to 50 °C). However, fluoride bond utilization decreased significantly to only ≤ 3 C–F bonds per CFI molecule at higher concentrations and/or rates. This premature cell termination was postulated to arise from the deactivation of reduction intermediates during discharge by dimerization of partially defluorinated R_F radicals,^[17] which is exacerbated when mass transport in the catholyte is limited (e.g., high CFI concentration, rate, or catholyte viscosity), resulting in accumulation of intermediates near the electrode surface that triggers this pathway.

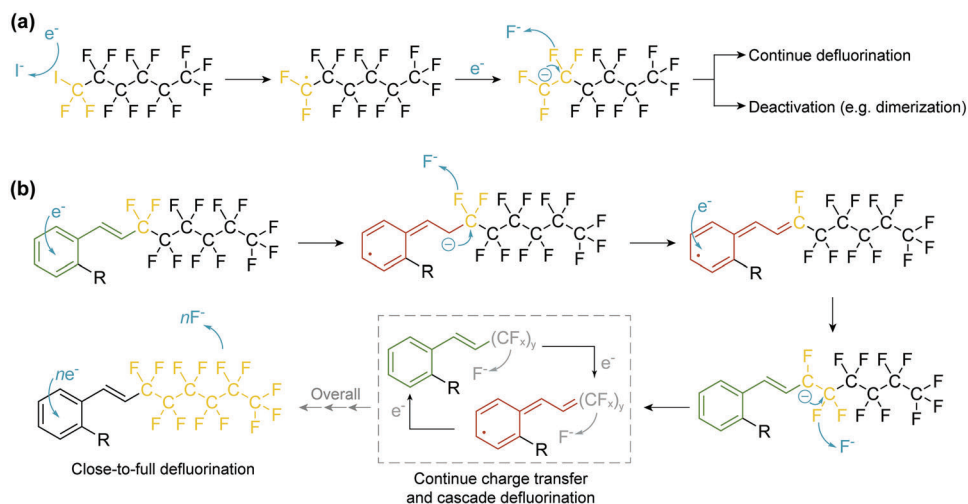
To overcome these limitations, herein, we report a new class of redox-active perfluoroalkanes designed to achieve extensive defluorination of R_F . Given the limitations observed with the –I-activated perfluoroalkanes, the terminal C–I bond was replaced with a stronger yet still polarizable bonding environment via a conjugated system (i.e., aromatic group) with an alkene linker to the perfluoroalkyl tail. This strategy gives rise to a versatile class of fluoroalkyl-aromatics that exhibit high electrochemical activities. Moreover, leading reactants among those examined here demonstrate an intrinsic ability to undergo close-to-full, cascade-like defluorination of R_F (up to 11/13 or 15/17 available F) when discharged in Li–carbon cells at moderate concentrations (up to 1 M) and rates (0.04 mA cm^{-2}), exceeding the limit of any previously-known fluoro-alkane. Factors influencing accessible extent-of-discharge and cell-level energy characteristics, including molecular structure and concentration, are examined in detail.

2. Results and Discussion

The –I functionality in previously-studied CFI reactants plays a key role as an initiating redox-active center that facilitates defluorination along the R_F chain. We proposed that this process begins with the formation of fluorocarbon radical intermediates^[17a] as detailed in **Scheme 1a**. However, the radical is also prone to side reactions such as premature self-dimerization, which deactivates the intermediates and renders additional F inaccessible. Therefore, we replaced the –I with a different functionality that undergoes less drastic structural change upon charge transfer: an aromatic, herein a phenyl (*Ph*) or pyridine (*Py*) ring, along with an alkene linker. We hypothesized that this conjugated system would function as the electron acceptor, substantially increasing the electron density near R_F (**Scheme 1b**). A delocalized radical anion can then trigger C–F bond cleavage, leaving a radical-like site that promotes the activation of adjacent C–F bonds. With the conjugated system continuously accepting and transferring electrons, the defluorination/activation can be driven down the R_F tail in a cascading manner. Two different R_F chain lengths were examined: $-\text{C}_6\text{F}_{13}$ (termed “C6”) and $-\text{C}_8\text{F}_{17}$ (C8). Additionally, a substituent functionality, *R*, on the ring structure enables further tuning of the electronic structure around R_F . These fluoroalkyl-aromatics, which are termed *R-Ph(or Py)-C6 (or C8)* (**Figure 1a**), were synthesized following a one-step Heck reaction using commercial precursors as reported in Ref. [18]. The lowest unoccupied molecular orbital (LUMO) of these molecules is centered on the conjugated alkene-aromatic group (**Figure S1**, Supporting Information).

The investigated reactants in **Figure 1** with long R_F chains (*p*-CN-Ph-C8 and *o*-NO₂-Ph-C8) or *para*-substituted *R* functionality (*p*-CN-Ph-C6) are solids at room temperature, while the others are liquid; all are soluble in organic solvents (**Table S1**, Supporting Information). None of the reactants could dissolve common lithium salts in their neat form, making it essential to include the supporting co-solvent. After preliminary screening, DMSO was chosen without optimization given its previously-demonstrated ability to promote LiF solvation and high capacities in other LiF-forming conversion batteries.^[16,19] Lithium perchlorate (LiClO_4) was used as salt to avoid additional F sources for characterization purposes. Cells were assembled using Li metal anodes, the as-described catholyte (fluoroalkyl-aromatics in 0.1 M LiClO_4 /DMSO), and a carbon cathode consisting of Ketjen black-coated on Toray paper (KB, 12 mm-diameter, unless otherwise noted).

Figure 1b examines the intrinsic redox behavior under galvanostatic conditions in Li cells containing 0.1 M of fluoroalkyl-aromatics at 0.04 mA cm^{-2} as a function of electrons transferred per reactant molecule (calculation details in Supporting Information), while **Figure 1c** presents a normalization to the reactant mass. To overcome limited solubility of long alkyl chain molecules (e.g., *p*-CN-Ph-C8) at room temperature, cells were tested at 50 °C unless otherwise noted. All reactants discharge via a single plateau with voltages ranging from 2.1 to $\approx 2.6 \text{ V}$ versus Li/Li⁺. The nitro (–NO₂) substituted reactants, *o*-NO₂-Ph-C6 and *o*-NO₂-Ph-C8, possess the highest discharge voltages of $\approx 2.6 \text{ V}$ versus Li/Li⁺, while those for cyano (–CN) substituted reactants (*o*-CN-Ph-C6, *p*-CN-Ph-C6, and *p*-CN-Ph-C8) are $\sim 0.1 \text{ V}$ lower. Reactants lacking an *R* group, Py-C6 and Ph-C6, show the lowest voltages at 2.2 and 2.1 V versus Li/Li⁺, respectively.



Scheme 1. Hypothesized defluorination pathway of a) perfluoroalkyl iodide (CFI)^[16] and b) fluoroalkyl-aromatics developed herein. The F⁻ intermediate generated would combine with Li⁺ in the catholyte and form LiF, while defluorinated organic fragments form as co-products.

Such change in discharge voltage is correlated to the electron-withdrawing strength of different *R* substituents, as described by the Hammett coefficient (Table S2, Supporting Information).^[20] In contrast to the *R* group, the R_F chain length had negligible impact on voltage, e.g., ≈2.6 V versus Li/Li⁺ for both *o*-NO₂-Ph-C6 and *o*-NO₂-Ph-C8. Instead, it most strongly impacted the discharge capacity, as seen by comparing the C6 and C8-containing reactants (Figure 1b). All C6 reactants (13 total F) exhibited capacities ranging between 10–12 e⁻/molecule, with ~11 typical of the higher-voltage *o*-CN-Ph-C6 and *o*-NO₂-Ph-C6, indicating

close-to-full defluorination of R_F. Meanwhile, the two C8 reactants (*o*-NO₂-Ph-C8 and *p*-CN-Rh-C8, 17 total F) achieved ≈14–15 e⁻ per molecule. Hence, reactant structures with longer alkyl chains tend to exhibit higher gravimetric capacities for an otherwise similar structure, for example, 642 and 681 mAh g⁻¹ reactant, respectively, at similar discharge voltage for *o*-NO₂-Ph-C6 and *o*-NO₂-Ph-C8, or 610 and 748 mAh g⁻¹ reactant for *p*-CN-Ph-C6 and *p*-CN-Ph-C8, respectively (Figure 1c). However, increasing the R_F chain length decreases the solubility of the reactants in DMSO (Table S1, Supporting Information). For example, *p*-CN-Ph-C6 is

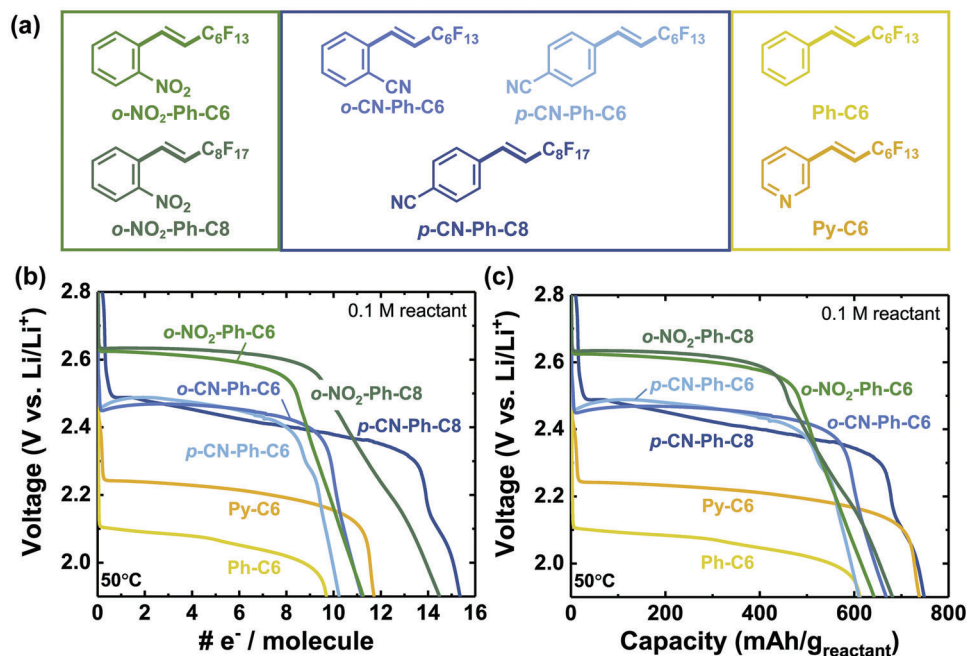


Figure 1. a) Molecular structures of fluoroalkyl-aromatic reactants, and their corresponding galvanostatic discharge profiles, with capacities normalized to b) number of electrons transferred per molecule or c) mass of the fluoroalkyl-aromatic reactants. Positioning of the *R* functionality relative to the perfluoroalkyl group (R_F) is denoted as *para* (*p*) or *ortho* (*o*). All cells were discharged at 50 °C and 0.04 mA cm⁻², with 0.1 M reactant in 0.1 M LiClO₄/DMSO electrolyte, in Li cells with Ketjen black (KB) cathodes.

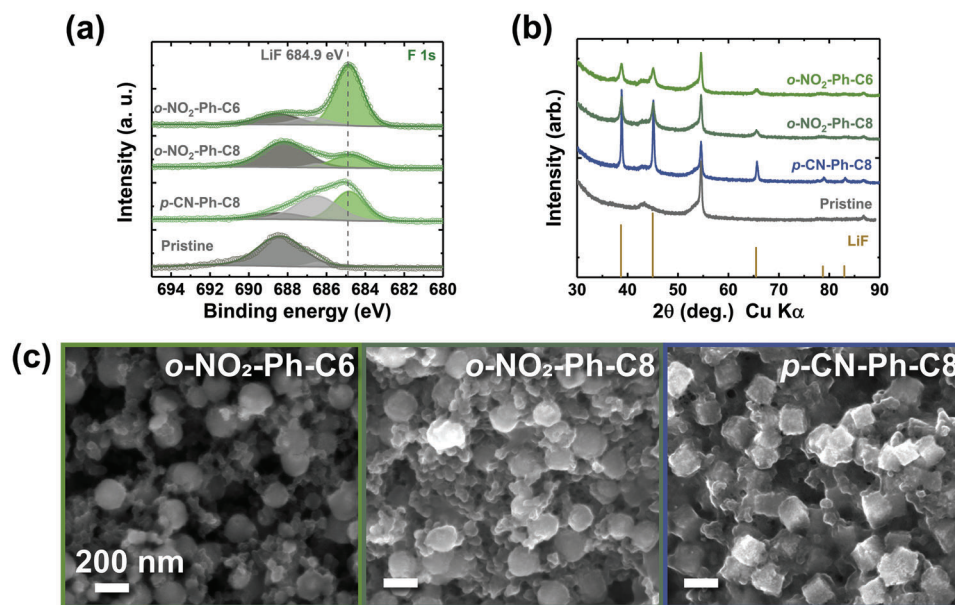


Figure 2. a) High-resolution F 1s XPS spectra of discharged KB electrodes from Li-*o*-NO₂-Ph-C6, *o*-NO₂-Ph-C8, and *p*-CN-Ph-C8 cells, with a fluoroalkyl-aromatic concentration of 0.1 M at 0.04 mA cm⁻² and 50 °C. The two C–F peaks at 688.4 and 686.4 eV are from the PVDF binder and/or PTFE-treated Toray paper substrate. The peak at 686.4 eV might also arise from partially defluorinated fluoroalkyl-aromatics, but further differentiation is not possible due to peak overlap. Some of the KB particles became detached from the cathode during cell disassembly, exposing more fluorinated binder and/or substrate (contains PTFE), contributing to the variability in relative peak intensities of non-LiF peaks. b) XRD and c) SEM of discharged KB cathodes from Li-fluoroalkyl-aromatics cells with 0.1 M reactant, discharged at 0.3 mA cm⁻² and 50 °C. Cell discharge capacities: 1.1, 1.5, and 1.5 mAh cm⁻², for *o*-NO₂-Ph-C6, *o*-NO₂-Ph-C8, and *p*-CN-Ph-C8, respectively.

liquid and miscible with DMSO at room temperature, but the C8 counterpart *p*-CN-Ph-C8 is solid and can only be solubilized at elevated temperature (solubility limit: 0.8 M at 50 °C). This indicates a trade-off between intrinsic capacity (per-molecule basis) and total active material loading (reactant concentration) that will inform practical cell design as discussed later. A potential handle to tune the reactant solubility is the *R* functional group (identity and position). For example, unlike *p*-CN-Ph-C8 which exhibits limited solubility, *o*-NO₂-Ph-C8 can reach a concentration of 2 M at room temperature. In contrast, for trifluoromethyl (–CF₃) substituted reactants, both *o*-CF₃-Ph-C6 and *p*-CF₃-Ph-C6 showed negligible miscibility with 0.1 M LiClO₄/DMSO even at 50 °C (Table S1, Supporting Information), thus the electrochemical properties of these molecules were not investigated herein.

All active molecules identified in this study contain the target reactive motif, R_F, plus a conjugated system with an alkene linker and an optional substituent *R*. We next tested the necessity of these components for accessing high degrees of defluorination. In contrast to Ph-C6, perfluorohexyl benzene (C₆H₅–C₆F₁₃), which lacks an alkene linker and substitutes R_F directly on the aromatic ring, exhibited negligible electrochemical activity on discharge (Figure S2a, Supporting Information), indicating that the alkene group is critical for facilitating the defluorination cascade propagating along the R_F tail. Similarly, reactants possessing only the alkene group + R_F (perfluorohexyl ethylene, CH₂=CH–C₆F₁₃), i.e., lacking the phenyl ring, were also electrochemically inactive (Figure S2b, Supporting Information), underscoring the importance of this constituent in promoting electron transfer. In addition, simply combining a benzonitrile aromatic (C₆H₅–CN) with CH₂=CH–C₆F₁₃ in the electrolyte again

yielded no activity (Figure S2c, Supporting Information), hence, we conclude that it is critical that these features be combined within the same molecule. Notably, these design guidelines appear to extend beyond the examined structures in Figure 1. Figure S3 (Supporting Information) shows similar discharge of the naphthalene-based fluoroalkyl-aromatic Naph-C6, containing an R_F substituent (C₁₀H₇–C₆F₁₃, Figure S3a, Supporting Information). Discharge capacities of up to 15 e⁻ per molecule were obtained, corresponding to 903 mAh g⁻¹ _{1-Naph-C6} at ≈2.0 V versus Li/Li⁺ (Figure S3b, Supporting Information).

Given their leading discharge performances in both voltage and capacity, cells containing 0.1 M of *o*-NO₂-Ph-C6, *o*-NO₂-Ph-C8, and *p*-CN-Ph-C8 reactants were further tested to examine the discharge reaction products. Using X-ray photoelectron spectroscopy (XPS, Figure 2a), all discharged cathodes indicated the emergence of a new peak at 684.9 eV corresponding to LiF in the F 1s high-resolution spectra,^[21] successfully confirming C–F bond reduction upon discharge. By X-ray diffraction (XRD), LiF was the only crystalline product detected for all three reactants (Figure 2b). The slightly lower peak intensity obtained with *o*-NO₂-Ph-C8 than *p*-CN-Ph-C8, despite the similar discharge capacities, is attributed to lower LiF crystallinity, as evidenced by round-edged LiF particles observable by scanning electron microscopy (SEM) for *o*-NO₂-Ph-C8(C6) compared to more clearly cubic LiF deposits for *p*-CN-Ph-C8 (Figure 2c). This suggests that the *R* functionality might influence LiF nucleation and growth even at relatively low reactant concentrations. Combining these results, we can conclude that the defluorination of R_F, i.e., C–F bond reduction, is a major reaction during discharge of Li-fluoroalkyl-aromatic cells.

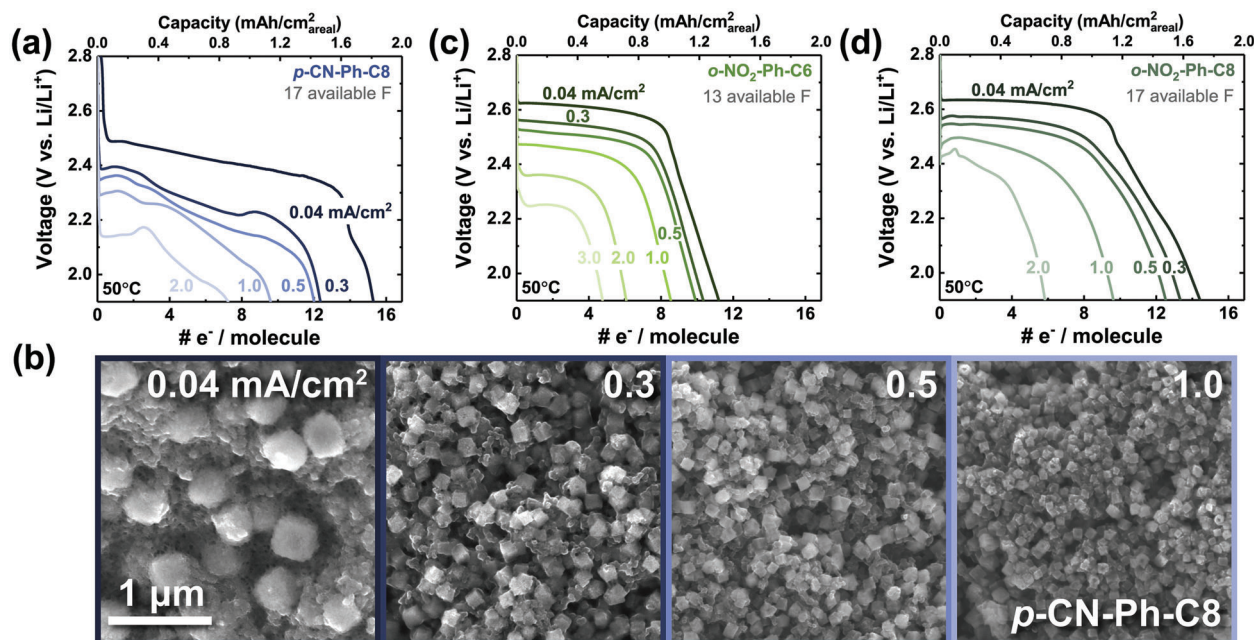


Figure 3. Galvanostatic discharge profiles of Li cells with 0.1 M fluoroalkyl-aromatic catholytes: a) *p*-CN-Ph-C8, c) *o*-NO₂-Ph-C6, and d) *o*-NO₂-Ph-C8 in 0.1 M LiClO₄/DMSO, with KB carbon cathodes (12 mm-diameter). b) SEM images of the KB electrodes after full discharge of Li-*p*-CN-Ph-C8 cells at 0.04, 0.3, 0.5, and 1.0 mA cm⁻² (as indicated). All cells were discharged at 50 °C.

The rate capabilities of the fluoroalkyl-aromatics at 0.1 M concentration were also investigated. Given its highest gravimetric capacity among all the reactants in Figure 1a, we first examined the discharge performance of *p*-CN-Ph-C8. As shown in Figure 3a, as the current density increases from 0.04 to 1.0 mA cm⁻², *p*-CN-Ph-C8 discharge capacity decreases from 15.3 to 9.5 e⁻ per molecule, accompanied by a ≈200 mV lower cell voltage. Further increasing the rate to 2.0 mA cm⁻² results in a significant voltage drop (to ≈2.1 V vs Li/Li⁺) with only 48% of the low-rate capacity attainable (7.3 e⁻ per molecule). To understand the potential origin of the capacity loss, we examined the rate-dependent LiF morphologies, which are shown in Figure 3b. As the current density increased from 0.04 to 1.0 mA cm⁻², the average LiF particle sizes decreased significantly from 257 ± 47 to 77 ± 25 nm, indicating less efficient carbon surface utilization at a high rate, which contributes to faster electrode passivation. Such decrease in LiF particle size at high current densities was also observed in other LiF-forming conversion batteries,^[19,22] which might be attributed to the increased driving force (e.g., higher concentration of F⁻ at the electrode/electrolyte interface due to higher reaction rate) towards LiF nucleation at high rates. A similar capacity decrease was also observed for the two nitro-substituted reactants (*o*-NO₂-Ph-C6 and *o*-NO₂-Ph-C8) in Figure 3c,d, where a capacity of ≈6 e⁻/molecule was obtained for both reactants at 2.0 mA cm⁻². Note that this number translates to better capacity retention (54%) for *o*-NO₂-Ph-C6 than *o*-NO₂-Ph-C8 (40%), due to a lower intrinsic (low-rate) capacity of *o*-NO₂-Ph-C6. As for voltage retention, both reactants exhibit a discharge voltage of ≈2.4 V versus Li/Li⁺ at 2.0 mA cm⁻², ≈300 mV higher than that obtained for the -CN-substituted reactants.

Given that practical battery applications favor a high active material loading to maximize the cell-level energy, we next in-

vestigated the effect of reactant concentration using *o*-NO₂-Ph-C₆ as a leading system (Figure 4). With KB carbon electrodes, a significant decrease in reactant utilization was observed (from ≈11.2 to 3.1 e⁻ per molecule) as the *o*-NO₂-Ph-C₆ concentration increased from 0.1 to 2.0 M. This might be attributable to premature LiF passivation at higher concentrations, and we hypothesized that discharge transitions from being reactant-limited (1.3 mAh cm⁻² at 0.1 M) to surface-limited (>7 mAh cm⁻² at 1–2 M,

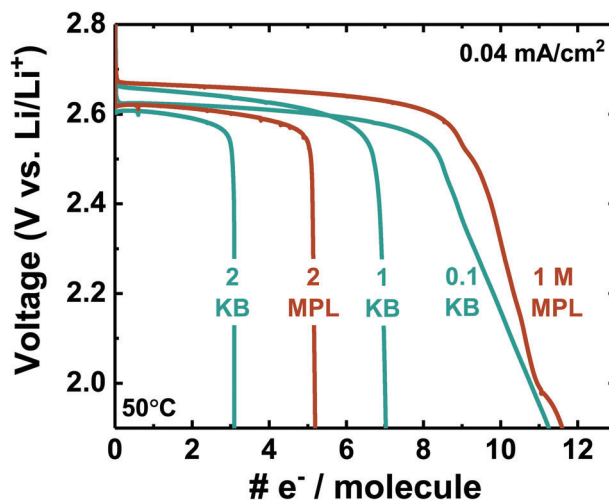


Figure 4. Galvanostatic discharge of Li-*o*-NO₂-Ph-C6 cells as a function of *o*-NO₂-Ph-C6 concentration at 0.04 mA cm⁻² with 12 mm KB cathodes (0.7 mg_C cm⁻²) and/or 15 mm microporous layer carbon substrates (MPL, 5 mg_C cm⁻²). All cells utilized 0.1 M LiClO₄ / DMSO as supporting electrolyte and were discharged at 50 °C. Capacities are normalized to the number of electrons transferred per *o*-NO₂-Ph-C6 molecule.

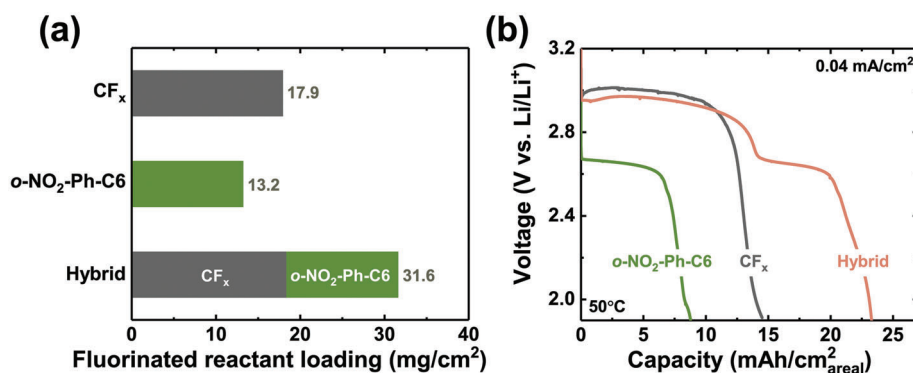


Figure 5. a) Active material loading, and b) galvanostatic discharge profiles of Li–CF_x, Li–o-NO₂-Ph-C6, and the hybrid cell. All cells utilized 15 mm diameter electrodes (CF_x or MPL), and were discharged at 0.04 mA cm⁻² at 50 °C. Both the Li–o-NO₂-Ph-C6 and hybrid cells used 1 M o-NO₂-Ph-C6 in 0.1 M LiClO₄/DMSO as catholyte.

Figure S4, Supporting Information), upon a 10–20× increase in active material loading. To test this hypothesis, we switched from KB electrodes (12 mm diameter, active carbon loading: ≈0.7 mg_C cm⁻²) to commercial microporous layer (MPL) carbon (see Experimental Section), which has a higher active carbon loading (5 mg_C cm⁻², 15 mm diameter). This cathode substrate change corresponds to an increase in total carbon from 0.8 to 8.9 mg per cell. As a result, full reactant utilization (≈11 e⁻ per molecule, as defined by the capacity obtained at 0.1 M and 0.04 mA cm⁻²) was achieved at a concentration of 1 M. Further increasing the reactant concentration to 2 M, however, again resulted in decreased reactant utilization (5.2 e⁻ per molecule), as well as ≈40 mV lower cell voltage. Beyond electrode passivation, this decreased utilization may also arise from the decrease in supporting solvent DMSO (≈62 wt.% at 1 M vs ≈31 wt.% at 2 M) leading to decreased LiF solubility and reduced catholyte transport properties (e.g., lower ionic conductivity).^[16,22] This challenge might be mitigated in the future by further increasing electrode surface area^[23] and/or utilizing supporting solvent with lower viscosity.^[16] Nevertheless, the close-to-full defluorination achieved at 1 M represents a significant improvement over the CFI system, where only <3 e⁻ per molecule were attainable at the same concentration, suggesting that replacing the –I functionality with a conjugated structure could effectively improve the stability of the reduction intermediates.

Another approach to improve the active material loading for practical cells is hybridization of solid and liquid cathodes. Such a hybrid cell design has recently been demonstrated in a Li cell with CF_x (solid) and pentafluorosulfanyl arene (liquid) cathodes, which successfully improved the gravimetric energy density of Li–CF_x cells by 20%.^[22] The energy gain mainly originated from the more efficient weight utilization in the cell, since the active catholyte replaces the traditional electrolyte in Li–CF_x cells (e.g., lithium tetrafluoroborate in propylene carbonate/dimethoxyethane),^[24] minimizing the weight of the inactive electrolyte solvent. Herein, we use o-NO₂-Ph-C6 to demonstrate the compatibility between fluoroalkyl-aromatics and CF_x solid cathode. As shown in **Figure 5a**, o-NO₂-Ph-C6/CF_x hybrid cells were fabricated with a CF_x cathode (loading of 18.4 ± 0.5 mg_{CFx} cm⁻², galvanostatic discharge profile in Figure S5, Supporting Information) and 50 μL of o-NO₂-Ph-C6 catholyte with a reactant concentration of 1 M (13.2 mg_{o-NO2-Ph-C6} cm⁻²). The

discharge profile of the hybrid cell exhibits two voltage plateaus (Figure 5b). The first plateau starts at 3.0 V versus Li/Li⁺ with a total areal capacity of 14.3 mAh cm⁻², similar to that obtained from Li–CF_x cells (14.5 mAh cm⁻²), with only ≈30 mV lower voltage that is attributable to the decreased transport properties of the catholyte compared to the 0.1 M LiClO₄/DMSO electrolyte in Li–CF_x. The voltage similarity suggests that the first plateau is mainly governed by reduction of solid CF_x. The second plateau exhibits a voltage of ≈2.7 V versus Li/Li⁺ and a capacity of 8.9 mAh cm⁻², very close to that obtained from the Li–o-NO₂-Ph-C6 cell (8.8 mAh cm⁻² at 2.7 V vs Li/Li⁺), indicating that the reduction of o-NO₂-Ph-C6 mainly occurs after CF_x discharge has completed. Note that both o-NO₂-Ph-C6 and CF_x exhibit a negligible capacity loss in the hybrid cell, demonstrating excellent chemical compatibility between the two electroactive components.

The cell-level energy/capacity metrics are analyzed and compared with CF_x- and CFI-only cathodes in Figure S6 and Table S3 (Supporting Information) at the sub-stack level, which includes the weight of electrodes and electrolyte (sub-stack = o-NO₂-Ph-C6 + CF_x + carbon + DMSO + consumed Li).^[22] Due to limitations in the assembly of lab-scale coin cells, an excess amount of electrolyte/catholyte is needed to ensure sufficient wetting of the solid cathodes, therefore both the CF_x and hybrid cell have a CF_x:liquid weight ratio of ≈0.5:1. This ratio is lower than that used in practical cells (CF_x:electrolyte ≈ 1:1 w/w in commercial Li–CF_x cell),^[25] and thus a higher sub-stack level energy can be projected for cells able to achieve optimized solid:liquid loading with the electrolyte/catholyte herein. For example, the attained energy density for a Li–CF_x cell with excess electrolyte is 695 Wh kg⁻¹_{sub-stack}, and is projected to reach 995 Wh kg⁻¹_{sub-stack} when the CF_x:electrolyte weight ratio reaches 1:1. In comparison, the attained gravimetric energy for a catholyte/solid hybrid cell with 1 M o-NO₂-Ph-C6 is 1050 Wh kg⁻¹_{sub-stack}, and is projected to further increase to 1345 Wh kg⁻¹_{sub-stack} under lean catholyte conditions, representing a 35% improvement over Li–CF_x. Achieving such ratios in practice requires advancements in methods for in-house cathode fabrication with higher loadings, and/or progression to pouch or cylindrical cells with vacuum sealing to reach higher solid-to-electrolyte ratios in future work.

In addition to the loading of fluorinated reactants, practical cell design may also require optimizing the fluoroalkyl-aromatic species based on the operating conditions. For example, different

power requirements will favor reactants with different fluoroalkyl chain lengths. Reactants with long R_F chains (C8) achieve the highest specific energies at low rates (e.g., at 0.04 mA cm⁻² and 0.1 M reactant concentration: 1695 and 1785 Wh kg⁻¹_{reactant} for *o*-NO₂-Ph-C8 and *p*-CN-Ph-C8, respectively, Figure S7a and Table S4, Supporting Information). However, at current densities ≥ 1 mA cm⁻², the shorter chain (*o*-NO₂-Ph-C6) reactants outperform the C8-containing analogues (e.g., at 1 mA cm⁻² and 0.1 M: 1165 Wh kg⁻¹_{reactant} for *o*-NO₂-Ph-C6 versus <1080 Wh kg⁻¹_{reactant} for the two C8 reactants, Figure S7b, Supporting Information). This suggests separate design strategies for batteries targeting high power or high energy applications, with long fluoroalkyl chain molecules more suitable for low rate and high energy, and short chain reactants being preferred when power requirement is more stringent. Temperature-dependent performance also needs to be taken into consideration. The room temperature (RT) rate performances were tested for the two nitro-substituted reactants, which are miscible/soluble with DMSO at RT, and the results are shown in Figure S8 (Supporting Information). At 0.04 mA cm⁻² with a reactant concentration of 0.1 M, both reactants exhibited slightly lower capacities than those obtained at 50 °C, with capacities of 10.4 and 12.8 e⁻ per molecule for *o*-NO₂-Ph-C6 and *o*-NO₂-Ph-C8, corresponding to gravimetric energy densities of 1470 and 1495 Wh kg⁻¹_{reactant}, respectively. Meanwhile, the rate capability advantage of the C6 molecule is more significant at RT: at 0.3 mA cm⁻² (with 0.1 M reactant), *o*-NO₂-Ph-C6 delivers a capacity of 9.3 e⁻ per molecule (1285 Wh kg⁻¹_{reactant}), while only 7.7 e⁻ per molecule (895 Wh kg⁻¹_{reactant}) was obtained from *o*-NO₂-Ph-C8 discharge. Overall, these findings indicate a viable strategy towards lower-temperature operations, which may be further improved by considering electrolyte co-design for higher reactant concentrations and lower viscosities in future work.

3. Conclusion

This study demonstrated the design principles for a new class of high-energy perfluoroalkylated catholyte reactants that enable close-to-full defluorination. These fluoroalkyl-aromatic reactants comprise three key components: an R_F tail, which is the major redox active component; a conjugated aromatic system with an alkene linker, which facilitates electron transfer and the reductive transformation propagating along the R_F tail; and an R functionality on the ring component that provides an additional handle to tune the R_F redox properties (e.g., reduction potential). When coupled with Li metal anodes, a remarkably high degree of R_F defluorination has been achieved (11/13 or 15/17 total available F), corresponding to >1.8 e⁻ per carbon (in R_F), and high gravimetric energy densities (up to 1785 Wh kg⁻¹_{reactant}), demonstrating the inherent potential in utilizing such reactant structures in Li batteries. The nitro group substituted fluoroalkyl-aromatics exhibit the highest discharge potential (≈ 2.6 V vs Li/Li⁺) and good solubility/miscibility in DMSO (up to 2 M), allowing the catholyte to function at moderate reactant concentrations (i.e., high active material loading). Moreover, the compatibility between fluoroalkyl-aromatics and CF_x enabled the design of a hybrid cell that utilized the reduction of fluorinated cathodes in both solid and liquid phases. Such hybridization is a promising approach to exceed the cell-level energy of Li-CF_x systems by minimizing the weight of electrochemically inac-

tive electrolyte solvent, with a 35% improvement projected with cell structure optimization. The system exhibits significant remaining room for further improvements, such as tuning the underlying ring structure and R functionality to increase the reduction potential and reactant solubility; utilizing high surface area cathode substrates to alleviate LiF passivation especially for concentrations > 1 M; balancing the solid-liquid ratio in the cell to maximize attainable capacities; and optimizing supporting solvent for improved transport properties. Overall, this class of perfluoro-alkylated catholytes opens up new opportunities to tailor the C-F bond activity and defluorination reaction pathways at a molecular structure level, providing a new platform for the design of high energy density Li primary batteries.

4. Experimental Section

Chemicals and Materials: All electrodes and cell-making materials were stored in an argon-filled glovebox (MBRAUN). The fluoroalkyl-aromatic reactants were synthesized with high yield from a one-step Heck reaction using commercial starting materials. The detailed synthesis methods are described in Ref. [18] LiClO₄ (99.99% trace metals basis, Sigma-Aldrich), stainless steel current collectors, stainless steel springs, and Whatman filter paper (Grade QM-A, 2.2 μ m pore size, 450 μ m thickness, Sigma-Aldrich) were dried in a Buchi glass oven under active vacuum overnight at 120 °C. Dimethyl sulfoxide (anhydrous, $\geq 99.9\%$, Sigma-Aldrich) and 1,2-dimethoxyethane (DME, anhydrous, 99.5%, inhibitor-free) were used as received and stored inside the glovebox.

Cathode Preparation: To fabricate the Kejten black (KB) electrodes used in Figures 1–4, KB (AzkoNobel) powder, *N*-Methyl-2-pyrrolidone (NMP), and polyvinylidene difluoride (PVDF) (with a weight ratio of carbon: PVDF = 80:20) were mixed together and sonicated to form a uniform ink. The carbon ink was then coated onto a sheet of Toray paper (polytetrafluoroethylene (PTFE)-treated, TGP-H-030, Fuel Cell Earth) using a doctor blade (MTI Corp.), and dried at room temperature. The obtained coated Toray paper was subsequently punched into circular disks (12 mm diameter) and dried under active vacuum in a glass oven (Buchi) overnight at 90 °C. Typical active carbon loading of KB electrodes is 0.73 \pm 0.08 mg cm⁻². The as-received microporous layer (MPL, 5 mg_C cm⁻², EQ-bcgdl-1400S-LD, MTI Corp.) used in Figure 4 and the Li-*o*-NO₂-Ph-C6 cells in Figure 5 were punched into 15 mm diameter disks and dried in Buchi oven at 90 °C overnight. CF_x electrodes used in Figure 5 (CF_x and hybrid cells) were fabricated in-house. CF_x powder ($x \approx 1.1$, Sigma-Aldrich), PVDF, Vulcan carbon (VC, XC-72, Cabot Corporation) (CF_x:PVDF:VC = 8:1:1), and NMP were mixed uniformly, rolled into a film, and dried at room temperature. The CF_x film was then pressed onto the stainless steel mesh (Dexmet), punched into 15 mm diameter disks and further dried at 120 °C overnight under vacuum in Buchi oven. Typical loading of CF_x is 18.4 \pm 0.5 mg cm⁻².

Galvanostatic Discharge: For cells with KB cathode substrates, two-electrode Swagelok-type cells were constructed in an Ar glovebox, with the dried KB cathode and a 9 mm diameter disk of Li metal as anode (0.75 mm thick, 99.9% metals basis, Alfa Aesar). The separator (13 mm diameter Whatman filter paper) was impregnated with 50 μ L fluoroalkyl-aromatic catholyte. Note that non-fluorinated salt (LiClO₄) was used to avoid additional fluorine sources, thus the only fluorine sources are fluoroalkyl-aromatics and PVDF/PTFE in KB electrodes. The latter two are well-known to be stable within the operating voltage window (1.9–3.0 V vs Li/Li⁺). For cells with MPL and CF_x cathodes, two-electrode coin cells were used. Cells were constructed inside the Ar glovebox with a 16 mm diameter Whatman separator, a 15 mm diameter Li anode, two stainless steel disks (MTI Corp.) as current collectors, and 50 μ L electrolyte/catholyte. An electric crimper (MSK-160E, MTI Corp.) with a constant mass loading of 0.82 tons was used for coin cell assembly. For galvanostatic discharge conducted at

50 °C, the cells were placed in an incubator (Memmert GmbH + Co. KG) after assembling. All cells were rested at open circuit voltage (OCV) for 5 h before prior to galvanostatic discharge. All discharge tests (BioLogic VMP3 potentiostat or MPG2 workstation) were conducted within a voltage window ranging from OCV to a lower voltage cutoff of 1.9 V versus Li/Li⁺. See Supporting Information for more details on cell structure and electrolyte/catholyte compositions.

Scanning Electron Microscopy (SEM): To harvest the discharged electrodes, the cell was disassembled inside the Ar glovebox and the cathode was extracted, rinsed with DME, and dried under vacuum at room temperature prior to SEM measurements. The dried cathode was sealed under Ar in a glass vial in glovebox. The sample was quickly transferred into the SEM chamber with minimal exposure to ambient. All SEM characterization was conducted on a Zeiss Merlin High-resolution SEM operating at an accelerating voltage of 5 kV and beam current of 100 pA.

X-Ray Diffraction (XRD): Discharged cathodes were rinsed with DME, dried under vacuum, and stored inside the glovebox. To minimize the exposure to ambient, samples were sealed in an air-sensitive sample holder under Ar inside the glovebox prior to XRD measurements. XRD patterns were collected on a PANalytical X'Pert Pro multipurpose diffractometer with a copper anode (Cu K α). All scans for cathode characterization were performed from 5° < 2 θ < 90° at a typical scan rate of 0.5° min⁻¹. Reference data for LiF: space group: *Fm* $\bar{3}$ *m*, JCPDS: 00-004-0857.

X-Ray Photoelectron Spectroscopy (XPS): Discharged cathodes were rinsed with DME, dried under vacuum, and sealed in an air-sensitive transfer vessel. XPS measurements were conducted on a PHI VersaProbe II X-ray Photoelectron Spectrometer. The binding energies were calibrated by the C–F binder peak (PVDF) at 688.40 eV. A Shirley-type background and a 70% Gaussian/30% Lorentzian line shape were used to deconvolute the high-resolution spectra using CasaXPS software.

Supporting Information

Supporting Information is available from the Wiley Online Library or from the author.

Acknowledgements

The authors gratefully acknowledge funding from the Army Research Office under award number W911NF-19-1-0311 and the National Science Foundation DMR-22-07299. This work made use of the MRSEC Shared Experimental Facilities at MIT, supported by the National Science Foundation under award number DMR-14-19807.

Conflict of Interest

The authors declare no conflict of interest.

Data Availability Statement

The data that support the findings of this study are available from the corresponding author upon reasonable request.

Keywords

carbon monofluoride, C–F bond activation, CF_x, Li–CF_x batteries, lithium batteries, primary batteries

Received: June 6, 2023

Revised: July 6, 2023

Published online: July 20, 2023

- [1] a) G. Pistoia, *Battery operated devices and systems: From portable electronics to industrial products*, Elsevier, Cham, Switzerland **2009**; b) J. Sather, in *Enabling the Internet of Things* (Ed: M. Alioto), Springer, Berlin, Germany **2017**, p. 409.
- [2] a) M. S. Whittingham, *Chem. Rev.* **2014**, *114*, 11414; b) N. Nitta, F. Wu, J. T. Lee, G. Yushin, M. Today, **2015**, *18*, 252.
- [3] W. Greatbatch, C. Holmes, E. Takeuchi, S. Ebel, *Pacing Clin Electro-physiol* **1996**, *19*, 1836.
- [4] A. Hills, N. Hampson, *J. Power Sources* **1988**, *24*, 253.
- [5] T. B. Reddy, D. Linden, in *Linden's Handbook of Batteries* (4th ed.), McGraw-Hill, New York **2010**, p. 141.
- [6] R. Schmich, R. Wagner, G. Hörpel, T. Placke, M. Winter, *Nat. Energy* **2018**, *3*, 267.
- [7] a) S. S. Zhang, D. Foster, J. Wolfenstine, J. Read, *J. Power Sources* **2009**, *187*, 233; b) J. Read, D. Foster, J. Wolfenstine, S. Zhang, *Army Res. Lab.* **2009**, <https://apps.dtic.mil/sti/pdfs/ADA588570.pdf>.
- [8] Q. Zhang, K. J. Takeuchi, E. S. Takeuchi, A. C. Marschillok, *Phys. Chem. Chem. Phys.* **2015**, *17*, 22504.
- [9] a) T. Nakajima, *J. Fluorine Chem.* **1999**, *100*, 57; b) K. Leung, N. B. Schorr, M. Mayer, T. N. Lambert, Y. S. Meng, K. L. Harrison, *Chem. Mater.* **2021**, *33*, 1760; c) B. Sayahpour, H. Hirsh, S. Bai, N. B. Schorr, T. N. Lambert, M. Mayer, W. Bao, D. Cheng, M. Zhang, K. Leung, K. L. Harrison, W. Li, Y. S. Meng, *Adv. Energy Mater.* **2022**, *12*, 2103196.
- [10] P. Lam, R. Yazami, *J. Power Sources* **2006**, *153*, 354.
- [11] N. Sharma, M. Dubois, K. Guérin, V. Pischella, S. Radescu, *Energy Technol.* **2021**, *9*, 2000605.
- [12] V. Mitkin, I. Asanov, L. Mazalov, *J. Struct. Chem.* **2002**, *43*, 843.
- [13] N. Watanabe, M. Fukuda, US Patent No. 3536532, **1970**.
- [14] T. Fuchigami, in *Electrochemistry Reactions of Fluoro Organic Compounds*, Springer, Berlin, Germany **1994**, pp. 1-37, https://doi.org/10.1007/3-540-57729-7_1.
- [15] a) D. Barker, D. Brewin, R. Dahm, L. Hoy, *Electrochim. Acta* **1978**, *23*, 1107; b) X. Q. Zhang, X. B. Cheng, X. Chen, C. Yan, Q. Zhang, *Adv. Funct. Mater.* **2017**, *27*, 1605989; c) X. Liu, J. Zhou, Z. Xu, Y. Wang, R. S. C. Adv, **2020**, *10*, 16302.
- [16] H. Gao, A. Sevilla, B. M. Gallant, *J. Electrochem. Soc.* **2022**, *169*, 030535.
- [17] a) C. P. Andrieux, L. Gelis, M. Medebielle, J. Pinson, J. M. Saveant, *J. Am. Chem. Soc.* **1990**, *112*, 3509; b) M. Médebielle, J. Pinson, J.-M. Savéant, *J. Am. Chem. Soc.* **1991**, *113*, 6872; c) C. Wakselman, *J. Fluorine Chem.* **1992**, *59*, 367.
- [18] a) K. Yoshinaga, T. M. Swager, *Synlett* **2021**, *32*, 1725; b) K. Yoshinaga, Massachusetts Institute of Technology, **2021**, <https://dspace.mit.edu/handle/1721.1/144091>.
- [19] H. Gao, Y. Li, R. Guo, B. M. Gallant, *Adv. Energy Mater.* **2019**, 1900393.
- [20] a) L. P. Hammett, *J. Am. Chem. Soc.* **1937**, *59*, 96; b) H. H. Jaffé, *Chem. Rev.* **1953**, *53*, 191.
- [21] A. V. Naumkin, A. Kraut-Vass, S. W. Gaarenstroom, C. J. Powell, *The NIST X-Ray Photoelectron Spectroscopy Database*, National Institute of Standards and Technology, Gaithersburg, MD **2000**.
- [22] H. Gao, A. Sevilla, G. M. Hobold, A. Melemed, R. Guo, S. C. Jones, B. M. Gallant, *Proc. Natl. Acad. Sci. USA* **2022**, *119*, e2121440119.
- [23] H. Gao, B. M. Gallant, *Nat. Rev. Chem.* **2020**, *4*, 566.
- [24] a) H. L. Seong, J. P. Ruiz, J.-P. Jones, J. Pasalic, K. Billings, W. West, R. Bugga, O. Crowther, M. Destephen, E. J. Brandon, *J. Electrochem. Soc.* **2022**, *169*, 060550; b) Y. Yin, J. Holoubek, A. Liu, B. Sayahpour, G. Raghavendran, G. Cai, B. Han, M. Mayer, N. B. Schorr, T. N. Lambert, *Adv. Mater.* **2023**, *35*, 2207932.
- [25] a) B. C. Muffoletto, R. J. Kuwik, U. S. Patent No. 5250373, **1993**; b) J. Probst, E. S. Takeuchi, S. A. Smesko, U.S. Patent No. 6451483, **2002**.